Tracking the structural evolution at atomic-scale in the spinel Mn_3O_4 induced by electrochemical cycling

X.Y. San, B. Zhang *, J. Wang, B. Wu, X.L. Ma

Shenyang National Laboratory for Materials Science, Institute of Metal Research, Chinese Academy of Sciences, Wenhua Road 72, 110016 Shenyang, China

ARTICLE INFO

ABSTRACT

Mn_3O_4 is a possible candidate for use as an electrode material and has been found to undergo structural transformation during electrochemical cycling. Clarifying the transformation process is important in developing methods for improving electrochemical performance. Here, using scanning transmission electron microscopy (STEM) combined with the electron energy loss spectroscopy (EELS) technique in aberration-corrected TEM, we succeeded in tracking the structural evolution at an atomic-scale and identified the intermediate stage as rock-salt-structured MnO. A reasonable route was deduced via which the spinel Mn_3O_4 was transformed firstly into MnO and then into MnO_2.

1. Introduction

Spinel transition metal oxides exhibit superior electrochemical performance characteristics in applications including energy conversion and storage systems, and for this reason are attracting considerable scientific attention [1,2]. Mn_3O_4 is a candidate electrode material for catalyzing the oxygen reduction reaction and electrochemical capacitance [3,4]. For many electrode materials in use, structural evolution usually occurs on the surface layer as electrochemical cycling takes place; this in turn has a strong influence on the resulting electrochemical properties [5–15], as demonstrated by changes in electrochemical performance. Clarifying the structural changes that occur in manganese oxides during cycling is therefore very important in improving their electrochemical performance. Previous studies have shown that Mn_3O_4 is converted into birnessite MnO_2 during voltammetric cycling in aqueous Na_2SO_4 electrolyte [16,17]. Although the final conversion product has been extensively studied by XRD, SEM and Raman scattering techniques, little attention has been given to the process by which this change occurs. Tracking the partially transformed state and capturing detailed structural and chemical information is key to identifying the intermediate products and further understanding the structural evolution of the spinel Mn_3O_4.

In the past few years, Fourier transform infrared spectroscopy (FTIR), synchrotron X-ray diffraction (XRD) and in situ X-ray absorption spectroscopy have been used to identify structural changes involving chemical bonds or lattice structures [18–21]. However, these methods are not very suitable for studying changes in structure and chemistry that occur at an atomic scale. Aberration-corrected HAADF (high angle annular dark field) STEM with EELS atomic resolution, on the other hand, is ideally suited for investigating structural transformations at sub-angstrom levels, capturing real-time direct images [22] which make it possible to monitor any structural changes taking place as a result of charge-discharge cycling [5–8,11,12].

Here we use an aberration-corrected TEM technique to study the structural evolution of Mn_3O_4 nanoparticles after voltammetric cycling in aqueous Na_2SO_4 electrolyte. The goal is to follow the changes in structure and chemistry, thus yielding new insights into the microstructure evolution process.

2. Materials and methods

Mn_3O_4 was synthesized by a hydrothermal method reported elsewhere [23]. $KMnO_4$ was used as the manganese source and polyethylene glycol (PEG200) as both reducing reagent and structure-directing agent to tailor the morphology of the Mn_3O_4 nanoparticles. The Mn_3O_4 powder was loaded onto a glassy carbon electrode with diameter of 3 mm (0.1 mg/cm^2), which served as the working electrode and then was treated via cyclic voltammetry (CV) in neutral 1 mol/L Na_2SO_4 electrolyte. CV was also performed on a blank glassy carbon electrode to confirm its electrical inactivity and the absence of measurable signal contributions. The samples subjected to CV were removed quickly from the glassy carbon electrode, then ultrasonically cleaned in ethyl alcohol, dried, and dispersed onto the amorphous carbon micro grid to produce TEM specimens. The as-synthesized Mn_3O_4 powder was also used to produce TEM specimens (blank samples). By observing the two types of specimens without and with CV treatments in the TEM, we can identify any structural changes.

* Corresponding author.
  E-mail address: bozhang@imr.ac.cn (B. Zhang).

A FEI-NOVA NanoSEM scanning electron microscope operated at 14 kV was used to characterize the morphology, a FEI-T12 transmission electron microscope was used for the electron diffraction studies and a Tecnai G2 F30 for the HRTEM imaging. An FEI-Titan G2 60–300 microscope with double aberration (Cs) correctors was used for HAADF-STEM imaging and EELS analysis. An energy dispersion of 0.25 eV/channel was used in the EELS spectra acquisitions, and a systemic energy resolution of 1.5 eV was selected according to the full width at half-magnitude of the zero loss peak.

A traditional three-electrode system was used in the CV measurements, in which the working electrode is the loaded Mn_3O_4, the counter electrode is Pt and reference electrode SCE (saturated with KCl). The electrolyte was 1 mol/L neutral $NaSO_4$. The potential scan ranged from -200 mV to 800 mV and the scan rate was 100 mV/s. An AUTOLAB PGSTAT302N electrochemical workstation was used in the CV measurements.

3. Results and discussion

Fig. 1, the SEM image, shows that most of the as-synthesized Mn_3O_4 particles have well-defined octahedral shapes. The octahedrons are irregular but tetragonally distorted due to the Jahn–Teller effect. Fig. 1b–d are the selected-area electron diffraction patterns (EDPs) indicating a tetragonal structure with lattice parameters a = b = 5.76 Å and c = 9.47 Å and space group I4$_1$/amd. Fig. 1e, the low-magnification (LM) bright-field (BF) TEM image, shows a typical rhomboid projection along the [100] direction of a nano-sized spinel octahedral-shaped Mn_3O_4 particle. Fig. 1f–g are the HRTEM and HRSTEM images along the [100] axis. The sharp and well-defined edge shown in the LMBF image is also valid at the atomic scale. The structure is obviously homogeneous and identical from surface to the interior, showing the typical atom projection arrangement of spinel.

The Mn_3O_4 working electrode was subjected to CV polarization in 1 mol/L Na_2SO_4 electrolyte and the voltammograms recorded. In the initial cycles, no apparent redox peaks appeared and the curves were flat loops. With more cycles, the flat loops became wider and well-defined redox peaks appeared. The two curves representing the 2nd and 2500th cycles are shown in Fig. 2a. The Mn_3O_4 after 2500 CV cycles was then observed in TEM, with particular focus on the changes in microstructure. The LM HAADF-STEM image (Fig. 2b) shows that most particles had been converted from an octahedral shape to highly porous fibroid nanoflakes after 2500 cycles. Some partially converted particles were still found to retain the octahedral shape but became porous, with blunted edges, as shown in Fig. 2c. We selected an edge zone in which only a slight contrast change was found, and obtained its HRTEM image (Fig. 2d). It can be seen that the structure of the surface (skin) layer was obviously different from that of the bulk material (main body). Obviously, the particle represents the fingerprint for the process of transformation. Through Fourier transform for the skin layer (indicated by a pink circle in Fig. 2d) and the main body area (indicated by a green circle), the main body was found to keep a tetragonal structure, whereas the reconstructed layer can be indexed as the [110] orientation of a face-centered cubic crystal structure (e.g. NaCl type), which is consistent with MnO. There thus exists an orientation relationship between $[110]_{MnO}//[100]_{Mn3O4}$ and $(-110)_{MnO}//(010)_{Mn3O4}$.

High-resolution HAADF-STEM imaging and EELS analysis were then employed to further examine the structure and chemistry of the reconstructed layer. The high-resolution HAADF-STEM image in Fig. 3a shows a well-defined reconstructed layer and a sharp interface. Representations of the atomic columns are shown in Fig. 3b, with the columns of Mn(III) cations (shown as green dots) occupying the octahedral sites and the columns of Mn(II) cations (purple dots) occupying the tetrahedral sites. The EELS analysis focusing on the valence state was performed on the main body and reconstructed layer. The full spectra
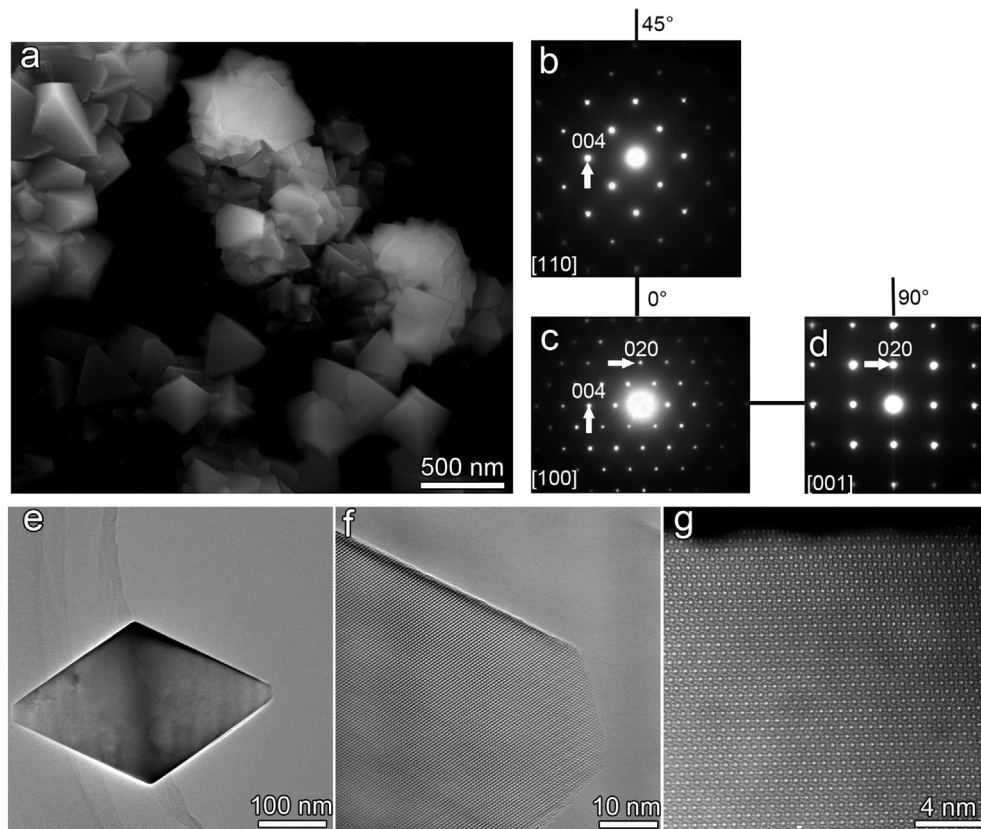

Fig. 1. Characterization of the as-synthesized Mn_3O_4 particles. (a) SEM image showing that the Mn_3O_4 particles have well-defined octahedral shapes. (b–d) EDPs along [110], [100] and [001] zone axis. (e) Low-magnification bright-field TEM image showing a typical rhombus shape of projection along [100] direction of a spinel octahedral-shape Mn_3O_4 nanoparticle. (f, g) HRTEM and high resolution HAADF-STEM image along [100] zone axis showing the edge is sharp and well-defined.
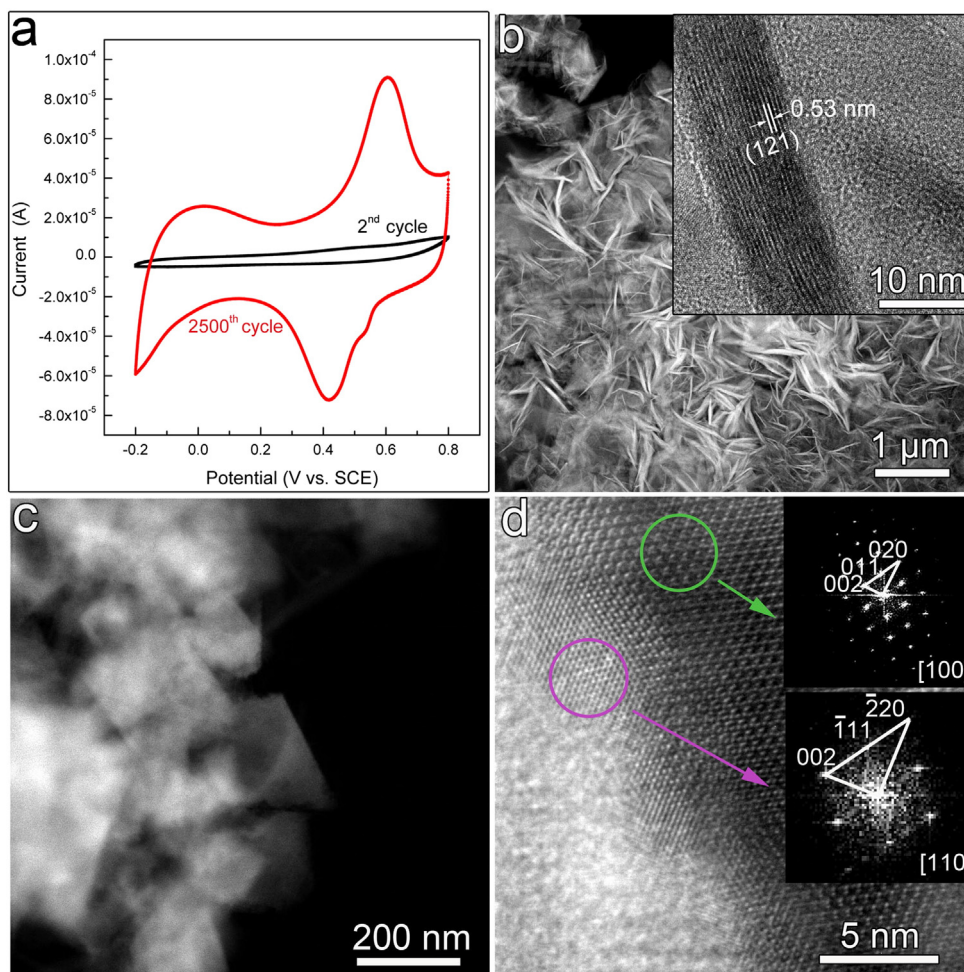
Fig. 2. The microstructural evolution of Mn_3O_4 after 2500 electrochemical cycles. (a) Cyclic voltammogram of Mn_3O_4 in 1 mol/L neutral Na_2SO_4 electrolyte at a potential scan rate of 100 mV/s after the 2nd and 2500th cycles. (b) The HAADF-STEM image illustrates that most particles have converted from the octahedral shape to highly porous fibroid nanoflakes after 2500 cycles. Inset is the HRTEM image of the fibroid nanoflake. (c) The TEM bright field image shows that some partially converted particles still keep an octahedral shape but have become porous and the edges have become ill-defined. (d) The HRTEM image obtained from the edge region of the partially converted particle along [100] direction. The insets are FFT images taken from the skin layer (pink circle) and the bulk (green circle). (For interpretation of the references to colour in this figure legend, the reader is referred to the web version of this article.)

covering the EELS edges from O to Mn are shown in Fig. 3c. The EELS data provide unambiguous recognition of the O K-edges and Mn-$L_{2,3}$ edges. The chemical shift to lower energy loss for the surface zone is evident, highlighting the evolution of the bonding or valence state in the reconstructed layer. Detailed views at an enlarged scale are shown in Fig. 3d (O-K edges) and Fig. 3e (Mn-$L_{2,3}$ edges). It is noteworthy that the EELS peak features of the O–K edges are more related to the geometry of the metal–oxygen bonding rather than the oxidation state, to which the transition metal is more sensitive [24,25]. As a result, the pre-peaks are usually observed at the lower energy side of the O-K edge (peak b) and take on alternating features with alternating bonding states. As shown in Fig. 3d, one pre-peak (peak a) of O-K exists in the EELS spectra obtained from the reconstructed region and two split peaks (peak a_1 and a_2) appear for the body region. The shift of the onset value of the energy loss and the change in white-line intensity ratio (L_3/L_2) are two essential indicators of valence state modification [26]. It is well known that the ionic edge of Mn has higher onset at higher oxidation states [25,27–29]. As shown in Fig. 3e, the onset values of energy loss of Mn-$L_{2,3}$ edges for the reconstructed layer are all shifted towards lower values compared with that of the full-body region, which point towards the relatively lower average valence of Mn in the reconstructed layer. The white-line intensity ratio (L_3/L_2), on the other hand, is closely related to the cation oxidation states [26]. Here we used two approaches – the double arctangent methods [30] and Pearson

method [31], and calculated the $L_{2,3}$ ratio to be 4.5 and 4.6 for the surface as well as 3.1 and 3.2 for the bulk body region. The evident increase of L_3/L_2 ratio in the reconstructed surface layer reflects the decrease of the average valence state of Mn, corresponding to MnO formation, which has a lower Mn valence (+2) than Mn_3O_4 (+3). The structural identification and the EELS analysis have therefore identified the intermediate product as MnO. In a similar way, the porous fibroid nanoflakes are identified as birnessite MnO_2 via the HRTEM (Fig. 2b insert) and EELS analysis (Fig. 3c–e).

Some previous reports [16,17,32] have suggested that the Mn_3O_4 electrode material transforms irreversibly into MnO_2 after a series of electrochemical cycles. A clear understanding of the detailed nature of the change was however lacking. In this study we have successfully tracked the partially-converted Mn_3O_4 particles, capturing structural and chemical information, and propose the following route for the transformation of Mn_3O_4 into MnO and finally to MnO_2. In the cathodic half-cycle, e.g. potential scanning from +0.8 V to −0.2 V, the spinel Mn_3O_4 undergoes electrochemical reduction, yielding rock-structured MnO. The reduction process should be a solid-solid transformation process since a sharp interface and good orientation interplay exist between the reconstruction layer and the full-body zone (as shown in Fig. 3a and b). Fetisov et al. had initially reported that the electrochemical reductive dissolution of Mn_3O_4 in acid solutions proceeded via solid phase reaction from Mn_3O_4 to MnO in the cathodic stage [33], though
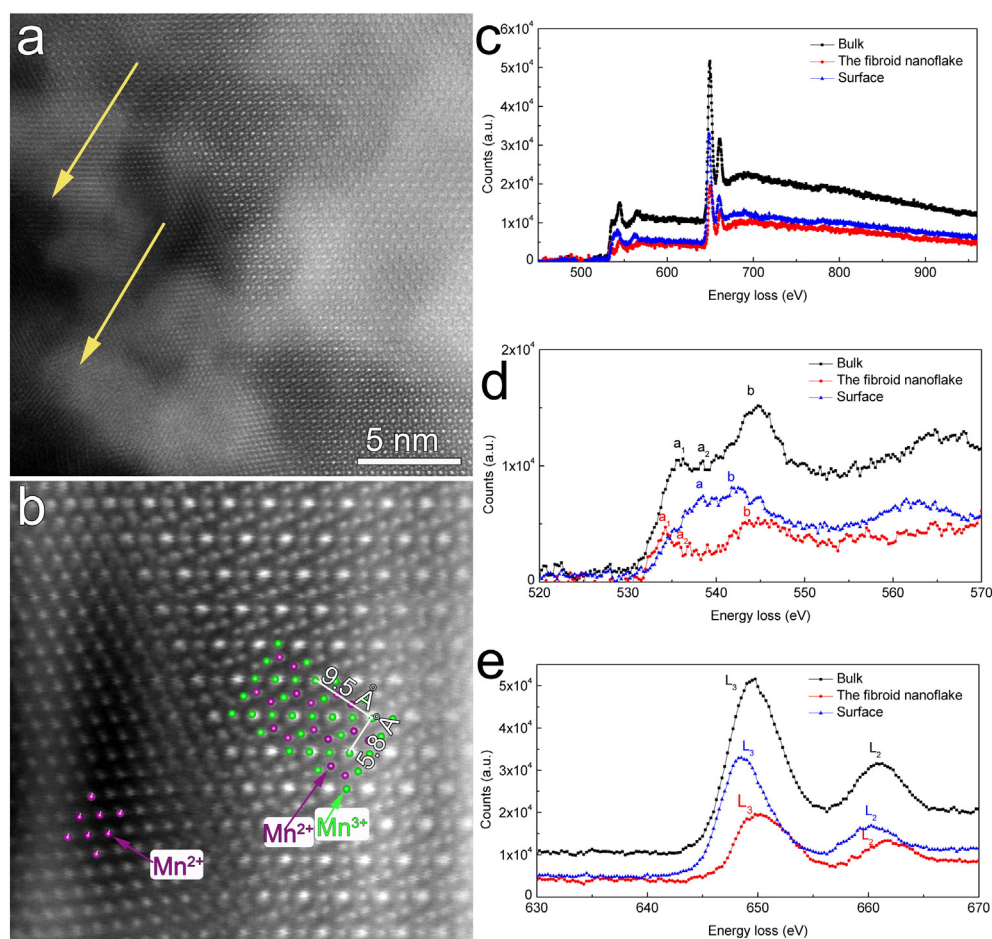
Fig. 3. The EELS analysis on the bulk, reconstruction layer and fibroid nanoflake region of the Mn_3O_4. (a) High resolution HAADF-STEM image showing a well-defined reconstruction skin layer and sharp interface. (b) The enlarged view of (a) illustrating the representations of the atom columns. The Mn (III) cation columns are represented by green dots and the Mn (II) cation columns by purple dots. (c) The full spectra covering the EELS edges from O to Mn. (d, e) Detailed views showing O K-edges and Mn-$L_{2,3}$ edges at an enlarged scale. (For interpretation of the references to colour in this figure legend, the reader is referred to the web version of this article.)

they did not perform any experiment to detect the existence of MnO. The MnO that accumulates on the surface during the cathodic processes is then chemically dissolved into Mn^{2+} (aq) and diffuses into the bulk of the electrolyte. A chemical dissolution process of this type is retarded in the cathodic half-cycle and accelerated in the anodic half-cycle, which can be explained in terms of charged-particle diffusion in an electric field [33]. As shown in Fig. 3a, the locations marked by yellow arrows become obscured and the bright atom columns become unobservable, indicating that the MnO reconstruction layer has undergone dissolution. Subsequently, the Mn^{2+} (aq) cations are electrochemically oxidized into the higher valence MnO_2 and re-deposited onto the surface. The dissolution-redeposition process yields the random fibroid products on display when the regular structural features fade and vanish as shown in Fig. 2b and c.

4. Conclusions

Using TEM combined with the EELS technique, we have succeeded in tracking the structural changes in spinel Mn_3O_4 nanoparticles at the atomic scale. After 2500 CV cycles in neutral Na_2SO_4 electrolyte, the octahedral-shaped Mn_3O_4 nanoparticles were fully transformed into highly porous fibroid MnO_2, whereas a well-oriented reconstruction skin layer was formed by the partially converted Mn_3O_4. The transformation from Mn_3O_4 to MnO involved a solid-solid transformation process, accomplished by electrochemical reduction during the cathodic stage. The final product, MnO_2, is produced by the dissolution-redeposition process occurring at the anodic stage.

Declaration of interest

The authors declare no competing financial interests.

References

[1] Y.Y. Liang, Y.G. Li, H.L. Wang, J.G. Zhou, J. Wang, T. Regier, H.J. Dai, Co_3O_4 nanocrystals on graphene as a synergistic catalyst for oxygen reduction reaction, Nat. Mater. 10 (2011) 780–786.
[2] A.K. Shukla, Q.M. Ramasse, C. Ophus, H. Duncan, F. Hage, G. Chen, Unravelling structural ambiguities in lithium-and manganese-rich transition metal oxides, Nat. Commun. 6 (2015) 8711.
[3] J.J. Duan, S. Chen, S. Dai, S.Z. Qiao, Shape control of Mn_3O_4 nanoparticles on nitrogen-doped graphene for enhanced oxygen reduction activity, Adv. Funct. Mater. 24 (2014) 2072–2078.
[4] J.W. Lee, A.S. Hall, J.D. Kim, T.E. Mallouk, A facile and template-free hydrothermal synthesis of Mn_3O_4 nanorods on graphene sheets for supercapacitor electrodes with long cycle stability, Chem. Mater. 24 (2012) 1158–1164.
[5] A. Boulineau, L. Simonin, J.-F. Colin, C. Bourbon, S. Patoux, First evidence of manganese–nickel segregation and densification upon cycling in Li-rich layered oxides for lithium batteries, Nano Lett. 13 (2013) 3857–3863.
[6] M. Gu, I. Belharouak, J.M. Zheng, H.M. Wu, J. Xiao, A. Genc, K. Amine, S. Thevuthasan, D.R. Baer, J.G. Zhang, N.D. Browning, J. Liu, C.M. Wang, Formation of the spinel phase

in the layered composite cathode used in Li-ion batteries, ACS Nano 7 (2012) 760–767.

[7] M. Gu, W. Shi, J.M. Zheng, P.F. Yan, J.G. Zhang, C.M. Wang, Probing the failure mechanism of nanoscale LiFePO$_4$ for Li-ion batteries, Appl. Phys. Lett. 106 (2015) 203902.

[8] R.M. Qiao, Y.S. Wang, P. Olalde Velasco, H. Li, Y.S. Hu, W.l. Yang, Direct evidence of gradient Mn (II) evolution at charged states in LiNi$_{0.5}$Mn$_{1.5}$O$_4$ electrodes with capacity fading, J. Power Sources 273 (2015) 1120–1126.

[9] Y.Y. Hu, Z.G. Liu, K.W. Nam, O.J. Borkiewicz, J. Cheng, X. Hua, M.T. Dunstan, X.Q. Yu, K.M. Wiaderek, L.S. Du, K.W. Chapman, P.J. Chupas, X.Q. Yang, C.P. Grey, Origin of additional capacities in metal oxide lithium-ion battery electrodes, Nat. Mater. 12 (2013) 1130–1136.

[10] C. Zhan, J. Lu, A.J. Kropf, T.P. Wu, A.N. Jansen, Y.K. Sun, X.P. Qiu, K. Amine, Mn (II) deposition on anodes and its effects on capacity fade in spinel lithium manganate-carbon systems, Nat. Commun. 4 (2013) 2437.

[11] C.D. Amos, M.A. Roldan, M. Varela, J.B. Goodenough, P.J. Ferreira, Revealing the reconstructed surface of Li[Mn$_2$]O$_4$, Nano Lett. 16 (2016) 2899–2906.

[12] F. Lin, I.M. Markus, D. Nordlund, T.-C. Weng, M.D. Asta, H.L. Xin, M.M. Doeff, Surface reconstruction and chemical evolution of stoichiometric layered cathode materials for lithium-ion batteries, Nat. Commun. 5 (2014) 3529.

[13] J.-H. Myung, D. Neagu, D.N. Miller, J.T.S. Irvine, Switching on electrocatalytic activity in solid oxide cells, Nature (2016) 528–531.

[14] Z. Du, H. Zhao, S. Yi, Q. Xia, Y. Gong, Y. Zhang, X. Cheng, Y. Li, L. Gu, K. Swierczek, High-performance anode material Sr$_2$FeMo$_{0.65}$Ni$_{0.35}$O$_6$-δ with in situ exsolved nanoparticle catalyst, ACS Nano (2016), http://dx.doi.org/10.1021/acsnano.6b03979.

[15] W. Zhang, W.T. Zheng, Exsolution-mimic heterogeneous surfaces: towards unlimited catalyst design, ChemCatChem 7 (2015) 48–50.

[16] D.P. Dubal, D.S. Dhawale, R.R. Salunkhe, C.D. Lokhande, Conversion of chemically prepared interlocked cubelike Mn$_3$O$_4$ to birnessite MnO$_2$ using electrochemical cycling, J. Electrochem. Soc. 157 (2010) A812–A817.

[17] Y. Dai, K. Wang, J.Y. Xie, From spinel Mn$_3$O$_4$ to layered nanoarchitectures using electrochemical cycling and the distinctive pseudocapacitive behavior, Appl. Phys. Lett. 90 (2007) 104102.

[18] Y. Gorlin, B. Lassalle Kaiser, J.D. Benck, S. Gul, S.M. Webb, V.K. Yachandra, J. Yano, T.F. Jaramillo, In situ X-ray absorption spectroscopy investigation of a bifunctional manganese oxide catalyst with high activity for electrochemical water oxidation and oxygen reduction, J. Am. Chem. Soc. 135 (2013) 8525–8534.

[19] K. Kubobuchi, M. Mogi, H. Ikeno, I. Tanaka, H. Imai, T. Mizoguchi, Mn L$_{2,3}$-edge X-ray absorption spectroscopic studies on charge-discharge mechanism of Li$_2$MnO$_3$, Appl. Phys. Lett. 104 (2014) 053906.

[20] S. Rabiei, D.E. Miser, J.A. Lipscomb, K. Saoud, S. Gedevanishvili, F. Rasouli, Conversion of hausmanite (Mn$_3$O$_4$) particles to nano-fibrous manganite (MnOOH) at ambient conditions, J. Mater. Sci. 40 (2005) 4995–4998.

[21] Y.S. Wang, X.Q. Yu, S.Y. Xu, J.M. Bai, R.J. Xiao, Y.-S. Hu, H. Li, X.-Q. Yang, L.Q. Chen, X.J. Huang, A zero-strain layered metal oxide as the negative electrode for long-life sodium-ion batteries, Nat. Commun. 4 (2013) 2365.

[22] H. Tan, S. Turner, E. Yücelen, J. Verbeeck, G. Van Tendeloo, 2D atomic mapping of oxidation states in transition metal oxides by scanning transmission electron microscopy and electron energy-loss spectroscopy, Phys. Rev. Lett. 107 (2011) 107602.

[23] Y. Li, H.Y. Tan, X.Y. Yang, B. Goris, J. Verbeeck, S. Bals, P. Colson, R. Cloots, G. Van Tendeloo, B.L. Su, Well shaped Mn$_3$O$_4$ nano-octahedra with anomalous magnetic behavior and enhanced photodecomposition properties, Small 7 (2011) 475–483.

[24] H.Y. Tan, J. Verbeeck, A. Abakumov, G. Van Tendeloo, Oxidation state and chemical shift investigation in transition metal oxides by EELS, Ultramicroscopy 116 (2012) 24–33.

[25] H. Kurata, C. Colliex, Electron-energy-loss core-edge structures in manganese oxides, Phys. Rev. B 48 (1993) 2102.

[26] Z.L. Wang, J.S. Yin, Y.D. Jiang, EELS analysis of cation valence states and oxygen vacancies in magnetic oxides, Micron 31 (2000) 571–580.

[27] J.H. Hwang, D.H. Kim, J.S. Kang, S. Kolesnik, O. Chmaissem, J. Mais, B. Dabrowski, J. Baik, H.J. Shin, J. Lee, Soft x-ray absorption spectroscopy study of Mo-rich SrMn$_{1 - x}$Mo$_x$O$_3$(x ⩾ 0.5), Phys. Rev. B 83 (2011) 073103.

[28] J. Lee, B. Kim, B.H. Kim, B.I. Min, S. Kolesnik, O. Chmaissem, J. Mais, B. Dabrowski, H.J. Shin, D.H. Kim, H.J. Lee, J.-S. Kang, Valence-state transition in SrMn$_{1 - x}$Mo$_x$O$_3$(0 ⩽ x ⩽ 0.5) investigated by soft x-ray absorption spectroscopy, Phys. Rev. B 80 (2009) 205112.

[29] M. Varela, M.P. Oxley, W. Luo, J. Tao, M. Watanabe, A.R. Lupini, S.T. Pantelides, S.J. Pennycook, Atomic-resolution imaging of oxidation states in manganites, Phys. Rev. B 79 (2009) 085117.

[30] P.A. Van Aken, B. Liebscher, Quantification of ferrous/ferric ratios in minerals: new evaluation schemes of Fe L$_{23}$ electron energy-loss near-edge spectra, Phys. Chem. Miner. 29 (2002) 188–200.

[31] D.H. Pearson, C.C. Ahn, B. Fultz, White lines and d-electron occupancies for the 3d and 4d transition metals, Phys. Rev. B 47 (1993) 8471.

[32] H. Xia, Y.S. Meng, X.G. Li, G.L. Yuan, C. Cui, Porous manganese oxide generated from lithiation/delithiation with improved electrochemical oxidation for supercapacitors, J. Mater. Chem. 21 (2011) 15521–15526.

[33] V.B. Fetisov, G.A. Kozhina, A.N. Ermakov, A.V. Fetisov, E.G. Miroshnikova, Electrochemical dissolution of Mn$_3$O$_4$ in acid solutions, J. Solid State Electrochem. 11 (2007) 1205–1210.